PAPER

Check for updates

Rapid parallel generation of a fluorescently barcoded drop library from a microtiter plate using the plate-interfacing parallel encapsulation (PIPE) chip†

Geoffrey K. Zath, [iD] ‡[ab] Ralph A. Sperling,‡[de] Carter W. Hoffman, [iD] [abc]
Dimitri A. Bikos, [iD] [ab] Reha Abbasi, [iD] [ab] Adam R. Abate, [iD] [f]
David A. Weitz [iD] [dg] and Connie B. Chang [iD] *[abc]

In drop-based microfluidics, an aqueous sample is partitioned into drops using individual pump sources that drive water and oil into a drop-making device. Parallelization of drop-making devices is necessary to achieve high-throughput screening of multiple experimental conditions, especially in time-sensitive studies. Here, we present the plate-interfacing parallel encapsulation (PIPE) chip, a microfluidic chip designed to generate 50 to 90 μm diameter drops of up to 96 different conditions in parallel by interfacing individual drop makers with a standard 384-well microtiter plate. The PIPE chip is used to generate two types of optically barcoded drop libraries consisting of two-color fluorescent particle combinations: a library of 24 microbead barcodes and a library of 192 quantum dot barcodes. Barcoded combinations in the drop libraries are rapidly measured within a microfluidic device using fluorescence detection and distinct barcoded populations in the fluorescence drop data are identified using DBSCAN data clustering. Signal analysis reveals that particle size defines the source of dominant noise present in the fluorescence intensity distributions of the barcoded drop populations, arising from Poisson loading for microbeads and shot noise for quantum dots. A barcoded population from a drop library is isolated using fluorescence-activated drop sorting, enabling downstream analysis of drop contents. The PIPE chip can improve multiplexed high-throughput assays by enabling simultaneous encapsulation of barcoded samples stored in a microtiter plate and reducing sample preparation time.

[a] *Center for Biofilm Engineering, Montana State University, Bozeman, MT, USA. E-mail: conniebchang@gmail.com*

[b] *Department of Chemical and Biological Engineering, Montana State University, Bozeman, MT, USA*

[c] *Department of Physiology and Biomedical Engineering, Mayo Clinic, Rochester, MN, USA*

[d] *Department of Physics, School of Engineering and Applied Sciences, Harvard University, Cambridge, MA, USA*

[e] *Fraunhofer Institute for Microengineering and Microsystems IMM, Mainz, Germany*

[f] *Department of Bioengineering and Therapeutic Sciences, University of California, San Francisco, CA, USA*

[g] *Wyss Institute for Biologically Inspired Engineering at Harvard University, Boston, MA, USA*

† Electronic supplementary information (ESI) available: Detailed device fabrication and additional experimental details. See DOI: https://doi.org/10.1039/d2lc00909a

‡ Authors contributed equally.

Introduction

Drop-based microfluidics technology reduces assay times and increases sample throughput by rapidly creating and analyzing picoliter-sized drops.[1,2] Drop-based microfluidics has recently been applied towards combinatorial drug discovery,[3] massively multiplexed nucleic acid detection,[4] and antibiotic susceptibility screening.[5] In these assays, 10^3 to 10^6 drops are tracked by a unique identifier in each drop, called a "barcode". This is commonly achieved using one of two barcode types: DNA barcodes introduced to tag drop contents as part of a next generation sequencing pipeline:[6–9] or fluorescent dyes and particles used to label drops for fluorescence-based assays, such as enzyme activity or dose–response screening.[3–5,10–14] DNA barcoding can provide upwards of 10^7 unique identifiers, enabling large-scale single-cell transcriptomics, but requires coalescing the drop emulsion before sequencing.[6–9] Though an advantage in single cell sequencing, drop coalescence prohibits ultrahigh-throughput experiments in which drop contents are assayed

over time. Fluorescent labeling allows the barcode and fluorescent assay output to be measured simultaneously without coalescing the drops. The resulting collections of either DNA or fluorescent barcodes in drops, known as "libraries", enable multiplexed or combinatorial readouts of the unique components encapsulated within the drops.[10–13]

A typical method for creating a barcode within a drop library is to emulsify a fixed sample volume of that barcode contained within a microtiter plate well or microcentrifuge tube using a single drop-making device. The process rapidly becomes labor- and time-intensive when a single drop-making device is used to generate increasingly large numbers of barcoded drops that are subsequently pooled together. Individual microfluidic drop makers can be run in parallel, but this requires multiple pump sources to emulsify each sample. Alternatively, liquid handling machines or autosamplers can be programmed to sequentially load individual samples from a microtiter plate into a microfluidic device;[14–17] however, these technologies are costly and cannot create multiple different barcodes simultaneously, which may be necessary for time-sensitive experiments. For example, all samples must be emulsified and processed in parallel to accurately capture the time-sensitive kinetics needed for performing comparative rapid enzymatic reaction screening studies.[18,19] Thus, to perform parallel encapsulation of multiple different barcodes, specialized microfluidic devices actuated using vacuum[20] or positive pressure[7,8] and containing multiple drop makers have been designed to interface with wells on standard microtiter plates. In prior work from Rotem et al., such a device was used to encapsulate DNA barcodes to perform single-cell chromatin profiling.[7,8] In this prior work, however, the fabrication of the device was not described in detail, nor was the device used to create fluorescently barcoded libraries. Extending the utility of this device for fluorescent barcoding would enable multiplexed assaying, wherein a barcoded signal is simultaneously measured along with an assay output. Additionally, fluorescently barcoded drops enable sample isolation and enrichment of a particular sample using fluorescence-activated drop sorting.[21,22] To allow for longer term storage of the drop libraries, fluorescent particles may be used in the place of dyes[3,11] to prevent diffusion of barcode labels between drops.[23]

Here, we detail the fabrication of a microfluidic device comprised of 96 simultaneously operating drop makers called the plate-interfacing parallel encapsulation (PIPE) chip that directly interfaces with 96 wells of a standard 384-well microtiter plate. The PIPE chip is operated within a pressure chamber, a modified commercial pressure cooker, wherein pressurized air drives parallelized drop formation across the 96 drop makers on the device. Parallelization enables rapid creation of drop libraries at a total drop throughput of approximately 300 kHz, approximately two orders of magnitude larger than serial drop generation using a single drop-making device, creating a total of approximately 3.6×10^7 drops in 2 min. Drop sizes produced by the PIPE chip are described using a simple drop scaling law, which allows for

fine-tuning of drop diameters ranging from approximately 50–90 μm. The PIPE chip is used to create two types of optically barcoded drop libraries using two-color combinations of either microbeads or quantum dots (QDs). A quarter of the 96 drop makers on the PIPE chip was used to create a drop library consisting of 24 fluorescent microbead combinations. The PIPE chip was also used twice to create a drop library consisting of 192 QD combinations. Fluorescence from each barcoded drop was measured at high speed using a flow-based detection method[22] to create a two-color scatter plot for each type of barcode library. A data clustering method, density-based spatial clustering of applications with noise (DBSCAN),[24] is used to identify uniquely barcoded concentrations and minimize the signal overlap between the combinations. The dominant sources of noise influencing the fluorescence signal overlap between barcode populations arise from Poisson loading for drops containing fluorescent microbeads approximately 1 μm in diameter and shot noise of the photodetector for drops containing QDs approximately 10 nm in diameter. The effect of these noise sources when designing barcode label concentration can be accounted for by scaling the barcode particle concentration with a quadratic function, thereby allowing for quick prototyping of barcode library labels. Finally, we demonstrate the utility of the PIPE chip by sorting and isolating a single fluorescently barcoded sample from a drop library of 24 different barcode combinations.[21,22] The ability to sort a specific barcoded sample from a drop library enables further analysis of drop contents using downstream techniques such as PCR amplification and genetic sequencing.[25–27] Drop libraries created with the PIPE chip can help to streamline existing multiplexed assays, such as combinatorial drug screening[3] or high-throughput assaying of protease activity,[12] by enabling simultaneous encapsulation of barcoded samples stored in a well plate.

Materials and methods

PIPE chip design

The PIPE chip was fabricated from three separate approximately 5 mm thick layers of polydimethylsiloxane (PDMS) plasma bonded on top of one another to form a 3-dimensional network of channels. The top layer of the device (Fig. 1a, i) is comprised of a narrow strip of PDMS containing two long channels that function as a common oil inlet and drop outlet for all three layers. Oil inlet and drop outlet channels run perpendicular to the channels in the remaining two PDMS layers, thereby allowing oil and drops to flow throughout the device from a single inlet and outlet, respectively. The oil inlet channel (Fig. 1a, i, blue) and drop outlet channel (Fig. 1a, i, yellow) are connected to the rest of the device through a total of nine via holes punched in the middle layer (Fig. 1a, ii), five for oil distribution and four for drop collection, providing a pathway for fluids from the top layer through to the bottom layer (Fig. 1a, dashed black lines). The middle layer contains oil distribution and drop collection
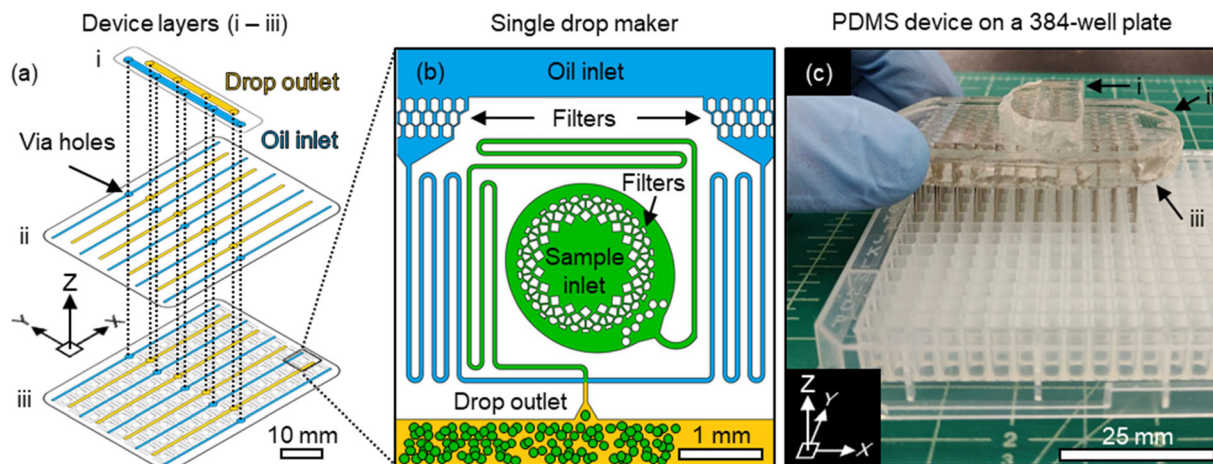
Fig. 1 PIPE chip design and assembly. (a) The PIPE chip was assembled from three layers: (i) a top layer containing oil distribution (blue) and drop collection (yellow) channels connected to a single inlet and outlet, respectively; (ii) a middle layer which reduces fluidic resistance by providing additional height to the oil and drop collection distribution channels on the bottom layer; and (iii) a bottom layer which contains an array of 96 drop makers (eight rows of twelve drop makers) with channels for oil distribution (five rows, blue) and drop collection (four rows, yellow). (b) Detailed view of one of the 96 drop makers positioned on the bottom layer. Colors are used to distinguish oil inlet (blue), aqueous sample inlet (green), and drop outlet (yellow) channels. (c) Image of a completed device interfaced with $\frac{1}{4}$ of a 384-well plate. Each layer (i–iii) of the fully assembled device from part (a) is indicated using black arrows. Stainless steel sample inlet capillary tubes are visible extending into the microtiter plate wells below.

channels that pass the oil phase to the drop makers and collect produced drops. The bottom layer (Fig. 1a, iii) contains 96 drop makers (Fig. 1b), each connected to oil distribution and drop collection channels. Drop maker inlet holes are spaced 4.5 mm apart to match the standard pitch of a 384-well microtiter plate, enabling the PIPE chip to interface directly to $\frac{1}{4}$ of a 384-well microtiter plate.

PIPE chip fabrication

Each of the PDMS layers i–iii (Fig. 1a) was cast from a unique master mold and bonded following standard techniques in soft lithography (see ESI† PIPE chip fabrication for details).[22] Short lengths (22.5 mm) of SAE 304 stainless steel capillary tubes (0.71 mm OD, 0.41 mm ID, Vita Needle) were fitted into the sample inlet holes of the device to provide a path for fluids from each microtiter plate well to the sample inlet of each drop maker (Fig. 1b). For encapsulating barcoded samples, the device was manually positioned above $\frac{1}{4}$ of a standard 384-well microtiter plate such that each of the stainless steel inlet capillaries nearly extended to the bottom of a different well (Fig. 1c).

Pressure chamber

The barcoded samples contained in the wells of the microtiter plate were simultaneously driven into each of the 96 drop makers of the PIPE chip under the uniform pressure within the sealed aluminum interior chamber of a 6-quart pressure cooker (Fig. 2a). Compressed air (approximately 60 psig) supplied both the oil reservoir pressure P_{oil} and chamber pressure P_{water}, both adjusted from 0–15 psig using manual regulators (McMaster-Carr 6745 K32 0–25 psi) and analog gauges (McMaster-Carr 3850 K2 0–15 psi). The oil

reservoir was comprised of a pressure-rated glass bottle (Sigma Duran Z674397) and a cap fitted with ports for compressed air and oil inlet tubing. Custom-drilled ports in the pressure chamber allowed the passage of oil inlet tubing and drop outlet tubing (Fig. 2a, side view). The ports were sealed with silicone sealant (DAP Kwik Seal Plus). A viewport was created using a 1.5 mm-thick transparent polycarbonate sheet that was affixed and sealed to a fabricated opening in the pressure chamber lid, allowing device operation to be monitored or recorded (Fig. 2a, top view). A strip of white LEDs (Ledmo SMD 2835) was mounted to the inside of the chamber to provide illumination.

Drop encapsulation

Barcoded samples were pipetted into individual wells of a 384-well microtiter plate and then placed into the pressure chamber apparatus. The PIPE chip was connected to the oil inlet and drop outlet tubing and positioned with the inlet capillaries extending into the wells of the microtiter plate containing barcoded samples (Fig. 2b). An oil reservoir was pressurized by house air and was regulated at pressure P_{oil} to control the oil flowrate. The oil reservoir contained Novec 7500 fluorinated oil (3 M) with 1.5% w/w of a Krytox-PEG surfactant that was synthesized in-house following a previously published protocol incorporating Jeffamine ED900 (Huntsman) as the hydrophilic portion of the PTFE–PEG–PTFE triblock perfluorosurfactant.[28] The water flowrate was controlled by a second regulator which adjusted P_{water} within the chamber, driving barcoded samples from each microtiter plate well into the PIPE chip to be encapsulated into drops. Barcoded drops were passed through the wall of the pressure chamber before reaching a collection tube to form a library of
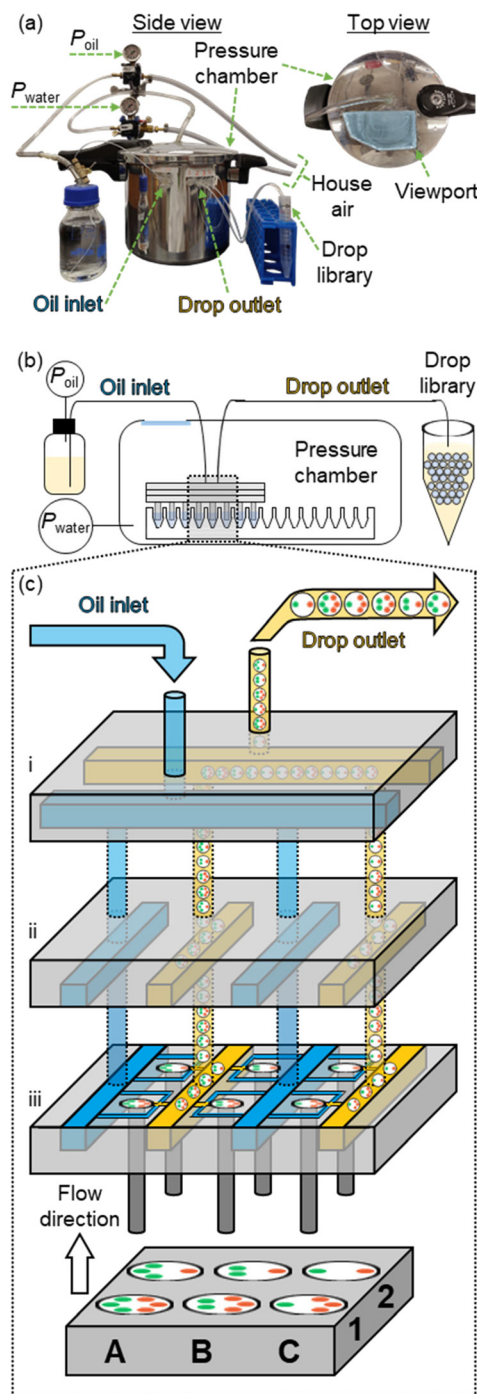
Fig. 2 PIPE chip operation and barcoded drop library production. (a) Side view and top view profiles of the PIPE chip apparatus and components. (b) PIPE chip operation schematic for the encapsulation of 96 wells from a 384-well microtiter plate. Pressure P_{oil} is applied to an external oil reservoir to provide oil to the device within the pressure chamber while a second pressure P_{water} applied to the chamber pushes fluid from sample wells into the microfluidic device. Barcoded drops travel through tubing past a sealed opening in the wall of the chamber for collection in a drop library. (c) Detailed schematic of the internal channels and flows within the PIPE chip. Samples in wells (indexed A–C and 1–2) barcoded with different concentrations of green and red microbeads are encapsulated in layer (iii), collected in large drop channels (yellow) formed from both layers (ii) and (iii) where they are transported to perpendicular drop collection channels in layer (i). The barcoded drops flow out of the device in a shared drop outlet.

drops, each indexed to a unique sample well. Drop collection continued for 2–3 min, or until air bubbles were observed in the outlet tubing, indicating sample wells were empty.

A detailed schematic summarizes barcoded drop encapsulation within the PIPE chip where barcoding is represented by a unique combination of green and red fluorescent microbead concentrations in each well (Fig. 2c). The encapsulation process is the same when quantum dots are used. Pressurization of the chamber pushes the fluid from these wells into the bottom PIPE chip layer (Fig. 2c, iii) where drops are formed at individual drop makers. The drops are then collected in shared drop outlet channels formed from the union of channels in the middle and bottom layer (Fig. 2c, ii and iii, yellow). These shared channels are connected to a perpendicular collection channel on the top layer (Fig. 2c, i) through via holes where drops subsequently flow and are collected in a common drop outlet. The flow of oil is the reverse of the flow of drops; a common oil inlet is distributed in the top layer (Fig. 2c, i) to perpendicular channels (Fig. 2c, ii and iii, blue) through via holes until oil reaches the drop makers (Fig. 2c, iii).

Drop size measurements

To characterize drop formation, the PIPE chip was placed on a petri dish filled with 10 mL of sterile-filtered deionized water (0.2 μm filter) within the pressure chamber and the oil reservoir was filled with 100 mL of Novec 7500 (3 M) oil with surfactant[28] added at 1.5% w/w. Drops were collected across a range of water P_{water} and oil P_{oil} inlet pressure combinations (2–3, 2–6, 2–12, 4–3, 6–3, 6–6, 6–12, 8–9, and 8–12 psig, where combinations are denoted as $P_{water} - P_{oil}$). Approximately 10 μL of drops were placed on an 8-well Teflon printed slide (Electron Microscopy Sciences, Cat. #63422-06) and imaged under an inverted brightfield microscope (Nikon TE2000). The height of the Teflon well was larger than the drop diameter, as drops regularly formed a bilayer during imaging. A custom image processing script in MATLAB (R2019a) was used to measure drop diameter D_{drop}. To convert the water and oil pressure ratios P_{water}/P_{oil} to volumetric flowrate ratios Q_{water}/Q_{oil}, we measured the volumes V of the oil and water phases after $t = 0.5$–2.5 min of collection for each water and oil pressure condition. In this case, surfactant was not added to the oil phase to allow for drop coalescence and phase separation of oil and water. The volumetric flowrates of each phase were calculated using $Q_i = \dfrac{V}{t}$ and plotted as Q_{water}/Q_{oil} as a function of P_{water}/P_{oil} (Fig. S1†).

Real-time drop formation within the PIPE chip was visualized through the viewport on the pressure cooker using a high-speed camera (Phantom VEO 710 L, Vision Research) attached to a tube lens (Model CFM, ISCO-OPTIC) mounted with a 10× objective (NA 0.25). The underside of the PIPE chip was illuminated by a liquid light guide routed through the side of the pressure cooker and attached to an LED light source (SugarCUBE, Ushio America).

Fluorescent microbead barcodes

Microbead barcodes consisted of unique two-color combinations of approximately 1 μm diameter green and red microbeads (Thermo Scientific Fluoro-Max G0100 ex. 468/em. 508 nm and R0100 ex. 542/em. 612 nm). Green and red microbead (stock of 1% solids, approximately 2.5×10^7 microbeads per μL) barcode labels were made from five dilutions in water (5.1×10^5, 1.3×10^6, 2.3×10^6, 3.6×10^6, 5.1×10^6 beads per μL). The five dilutions of each microbead color were mixed equally in a combinatorial manner to create a total of 24 barcode labels. The concentration combinations are detailed in Table S1.† Four concentrations of blue microbeads (Thermo Scientific Fluoro-Max B0100 ex. 412/em. 473 nm, 5.1×10^5, 1.3×10^6, 2.3×10^6, 3.6×10^6 microbeads per μL from a stock of 1% solids, approximately 2.5×10^7 microbeads per μL) were randomly spread across 24 microbead-barcoded wells and used as a mock assay signal. For microbead barcoded drop experiments, the oil pressure was set to 3 psig (P_{oil}) and the chamber pressure was set to 2 psig (P_{water}). For the purpose of collecting 24 samples instead of 96, a modification to the PIPE chip was made to allow drop outlet tubing to be directly connected to the drop collection channels of the second layer of the device. This modification provided separate collection from each quadrant of drop makers on the device where each quadrant is comprised of 24 drop makers. A confocal image of the microbead barcoded drops captured in a drop array device[29] is shown in Fig. S2.† The drop library was collected and re-injected into a secondary device for use with a custom drop fluorescence detection system (see ESI† Barcoded drop detection and Fig. S3 and S4 for details).[22] The photomultiplier tube (PMT) gain control voltage was set to 0.32 V for microbead barcoded drop detection.

Quantum dot barcodes

QDs of two colors (Thermo Scientific QD625 and QD705) were used as barcode labels by preparing 12 QD625 (1.15×10^4, 9.68×10^3, 8.00×10^3, 6.48×10^3, 5.12×10^3, 3.92×10^3, 2.88×10^3, 2.00×10^3, 1.28×10^3, 7.20×10^2, 3.20×10^2, 8.00×10^1 pM) and 16 QD705 (1.02×10^4, 9.00×10^3, 7.84×10^3, 6.76×10^3, 5.76×10^3, 4.84×10^3, 4.00×10^3, 3.24×10^3, 2.56×3, 1.96×10^3, 1.44×10^3, 1.00×10^3, 6.40×10^2, 3.60×10^2, 1.60×10^2, 4.00×10^1 pM) dilutions in 10 mM sodium borate buffer pH 9 containing 0.5 mg mL^{-1} bovine serum albumin (BSA). The 12 and 16 dilutions were mixed equally in a combinatorial manner to create a total of 192 barcode labels. The concentration combinations are detailed in Table S2.† For drops containing QD barcodes, the oil pressure (P_{oil}) was set to 8 psig while the chamber pressure (P_{water}) was set to 5 psig. The PIPE chip was operated twice to create 192 barcodes (96 × 2). The PMT control voltage was set to 0.45 V for QD barcoded drop detection.

Two-channel fluorescence-activated drop sorting

Barcoded drops were injected into a microfluidic drop sorting device[22] at a flowrate of 40 μL h^{-1} and spacer oil (Novec 7500) without surfactant was injected at a flowrate of 800 μL h^{-1}. A sorting electrode driven by a high voltage amplifier (Trek Model 2220-CE) and controlled by a custom LabVIEW program was used to pull drops into a collection channel. The sorting electrode provided a 400 μs pulse of a 25 kHz, 400 V square wave signal when the drop fluorescence signal fell within the threshold values set for a specific barcode (1–1.2 V green channel, 0.15–0.25 V red channel).

Results and discussion

Drop formation characterization

Drops were generated with the PIPE chip under a range of pressures for P_{water} and P_{oil} to identify combinations that produce uniformly-sized drops. We measured D_{drop} and its distribution, as quantified by the coefficient of variation (CV) of D_{drop}, at each pressure combination (Fig. 3a). To observe drop formation across the range of pressures tested, high speed videos of drop formation in the PIPE chip were captured at four extreme water and oil pressure combinations. The four combinations are labeled with corresponding symbols in Fig. 3a–c: high water pressure (■, P_{water} = 6 psig and P_{oil} = 3 psig), low combined pressure (▼, P_{water} = 2 psig and P_{oil} = 3 psig), high combined pressure (▲, P_{water} = 8 psig and P_{oil} = 12 psig) and high oil pressure (♦, P_{water} = 2 psig and P_{oil} = 12 psig). Representative images of Videos S1a–d† are presented in Fig. 3b. At high water pressure (■), the greater water volume fraction led to each drop filling the full length of the exit channel and partially extending into the collection channel before drop break-up occurred, a phenomenon not seen with the other three combinations. As drop formation is no longer fully constrained by the flow focusing junction, this extension of the drop into the collection channel may explain the greater polydispersity at this condition, where D_{drop} = 83.9 ± 12.5 μm. At low and high combined pressure conditions (▼, ▲, both at P_{water}/P_{oil} = 0.67), drop formation occurred within the exit channel, creating smaller, more uniform drops at the high pressure condition (▲, D_{drop} = 56.2 ± 2.6 μm) than the low pressure condition (▼, D_{drop} = 68.8 ± 5.0 μm). Drop uniformity did not improve with a higher oil volume fraction (♦, CV = 6.0%) when compared to the high combined pressure condition (▲, CV = 4.6%). As the oil volume fraction was increased, drop formation was limited by the 50 μm width of the exit channel, a characteristic of drop formation in the dripping regime.[30,31] The dripping regime forms highly uniform drops, whose diameters are largely determined by the flowrates and the width of the flow focusing junction.[30,32,33] For all the conditions observed, drop break-up occurred at the flow-focusing junction which indicates that drop formation was in the dripping regime.[30,32]

The size of drops formed in the dripping regime can be described by a drop scaling law,[34] thereby providing a predictive drop formation model for the PIPE chip. A drop scaling law[34] developed for T-junction geometries, and shown to be applicable for flow focusing geometries,[35] is fit to the data and defined as:
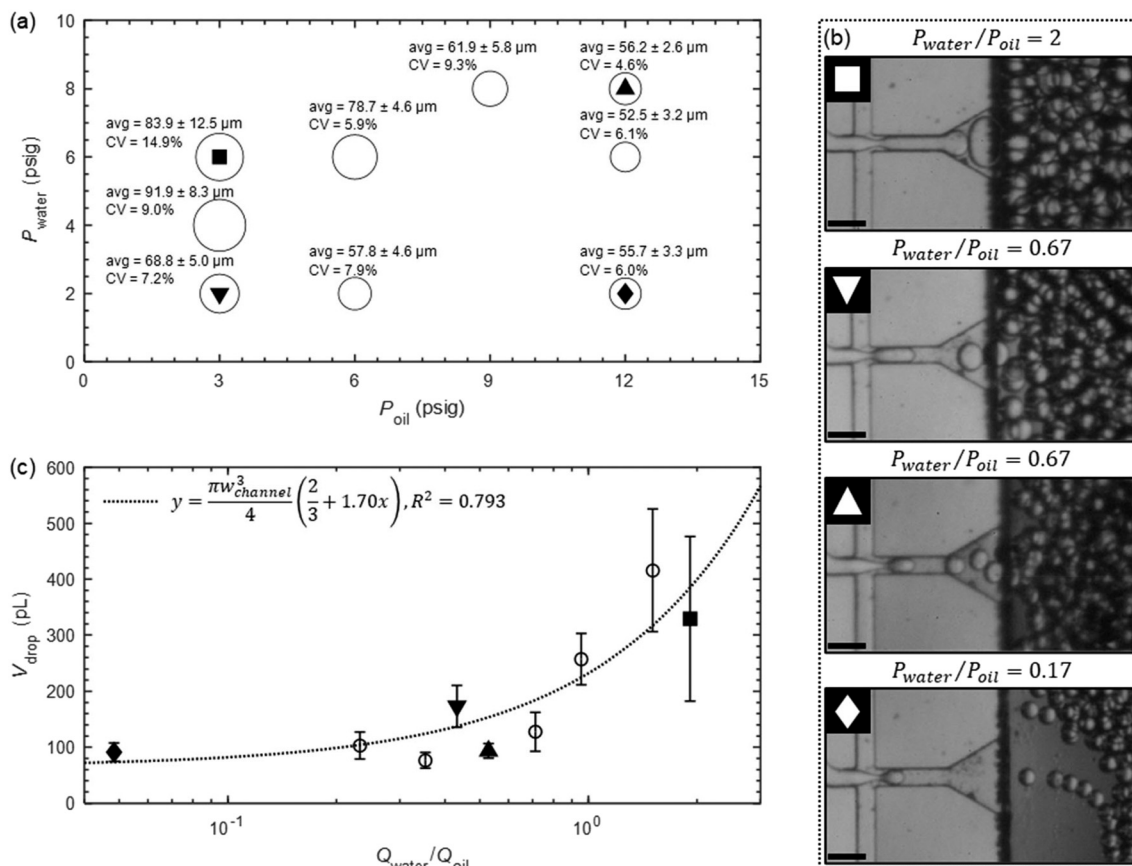
Fig. 3 Characterization of drop sizes produced by the PIPE chip. (a) Drop diameter average, standard deviation, and CV at various water pressures P_{water} and oil pressures P_{oil}. For additional visualization, the relative size of each open circle corresponds to the relative mean drop diameter measured. Solid shapes indicate conditions used for high-speed image capture in (b). (b) High-speed image capture of drop formation, ordered by descending D_{drop}, for high water pressure (■, P_{water} = 6 psig and P_{oil} = 3 psig, P_{water}/P_{oil} = 2), low combined pressure (▼, P_{water} = 2 psig and P_{oil} = 3 psig, P_{water}/P_{oil} = 0.67), high combined pressure (▲, P_{water} = 8 and P_{oil} = 12 psig, P_{water}/P_{oil} = 0.67), and high oil pressure (♦, P_{water} = 2 psig and P_{oil} = 12 psig, P_{water}/P_{oil} = 0.17) conditions. Scale bars = 100 μm. (c) Corresponding drop volumes V_{drop} versus the volumetric flowrate ratio Q_{water}/Q_{oil} (open circles or solid shapes). V_{drop} scales with Q_{water}/Q_{oil} following a drop scaling law (dotted black line).[34] Error bars represent one standard deviation from the mean.

$$\frac{L_{drop}}{w_{channel}} = 1 + \alpha \frac{Q_{water}}{Q_{oil}} \qquad (1)$$

where L_{drop} is defined as the length of a drop in the channel measured end to end, $w_{channel}$ is the width of the channel (50 μm), Q_{water}/Q_{oil} is the volumetric flowrate ratio, and α is a geometric constant of order 1. To apply the scaling law to our data, pressure ratios are converted to flowrate ratios using a standard curve (Fig. S1†). We converted L_{drop} from eqn (1) to drop volume V_{drop} by approximating the shape of the drop as a capsule geometry when drops are elongated within the microfluidic channel (see ESI† PIPE chip drop formation characterization for details). The best fit of the drop scaling law with V_{drop} plotted as a function of Q_{water}/Q_{oil} is presented as a dotted line in Fig. 3c with α = 1.70 and an R^2 = 0.793.[34] Drops produced using the PIPE chip can be adjusted by tuning the pressures applied to the oil and aqueous phases, thereby adjusting Q_{water}/Q_{oil} and enabling the generation of drops within a desired range of diameters (≈50–90 μm).

Drop size distribution improved from a CV of 14.9% to 4.6% as Q_{water}/Q_{oil} was decreased from 2 to 0.17 (Fig. 3c). When $Q_{water}/Q_{oil} < 1$, further reductions in Q_{water}/Q_{oil} have diminishing effects on V_{drop}. In this case, the minimum drop volume (65 pL, correlating to D_{drop} = 50 μm) is reached as $Q_{water}/Q_{oil} \rightarrow 0$ due to the 50 μm width of the drop channel ($L_{drop} \approx w_{channel}$ according to eqn (1)). Interestingly, despite the low and high combined pressure conditions having the same pressure ratio and similar measured flowrate ratios (Q_{water}/Q_{oil} = 0.43 or 0.53, respectively), they produced drops with different V_{drop}, from 173 ± 37 pL to 94 ± 13 pL. The difference in V_{drop} for similar Q_{water}/Q_{oil} at higher oil flowrates may be attributed to an increased oil phase capillary number Ca which represents the ratio of the viscous drag to surface tension forces acting on a drop. A higher oil phase Ca corresponds to increased drag at the drop formation junction which leads to faster break-up, resulting in a decreased V_{drop}.[30,35]

Optimizing barcode discrimination in drop libraries

Drop libraries barcoded with fluorescence-based barcodes have recently reached a label count of 1050 unique combinations with the use of four dye colors.[4] Lanthanide nanophosphors

are capable of creating up to 1023 unique labels with a six-color combination, but have yet to be used in drop libraries.[36] However, using a large number of barcode colors may not be advantageous, as the overlap of emission spectra between the fluorescent reporters can limit the practical number of colors that can be used in an assay.[37,38] Simply reducing the number of barcode colors to one or two and varying their concentrations can greatly expand the range of usable reporters. Thus, the PIPE chip was used to generate two fluorescently barcoded drop libraries from two-color combinations of either microbeads or QDs. Fluorescent particles were used to prevent diffusion of the barcode labels between drops.[23] The libraries were prepared by mixing

different ratios of each color to form distinct combinations on a microtiter plate (see Materials and methods). The polystyrene microbead drop library was comprised of 24 barcodes made from ratios of green and red fluorescent polystyrene microbeads while the QD drop library was comprised of 192 barcodes made from ratios of QDs with peak emissions at 625 and 705 nm. The PIPE chip was used to simultaneously encapsulate all the barcoded contents of the plate in 2 min, creating approximately 3.75×10^5 drops ($D_{\text{drop}} = 50$ μm) per barcode. Barcoded drops were reinjected into a microfluidic device for analysis using a laser-induced fluorescence detection system.[22] Drop fluorescence was measured as the drops flowed past a laser at approximately 300 Hz.
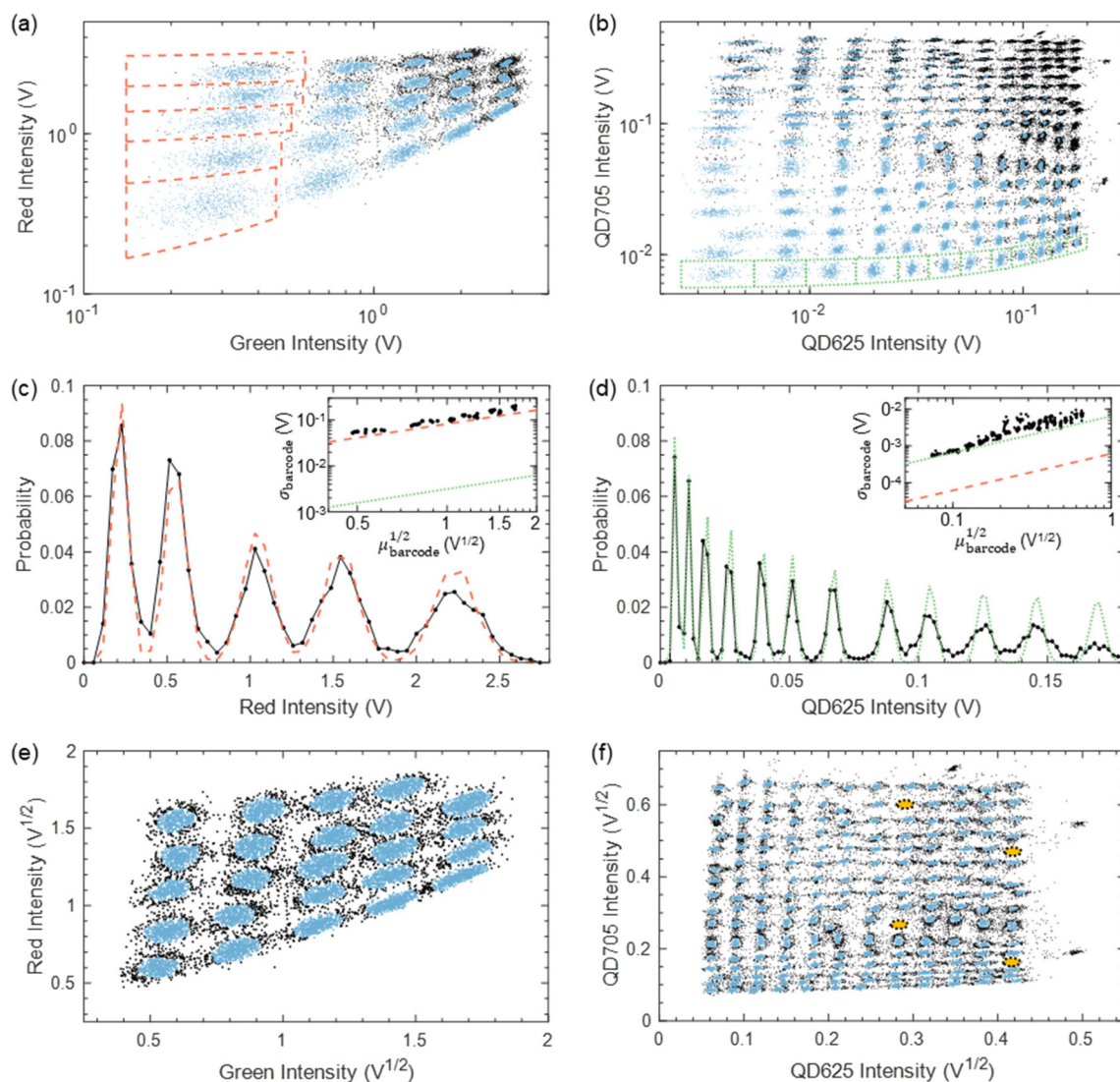

Fig. 4 Analysis of microbead and QD barcoded drop libraries. Scatter plots of (a) microbead and (b) QD fluorescence intensity in the drop library. Clusters identified by DBSCAN are indicated in blue while noise is in black. Probability distributions of (c) five red microbead barcoded drop populations (black dots) plotted against the particle loading noise estimate (dashed red line, $R^2 = 0.931$) and (d) twelve QD625 barcoded drop populations (black dots) plotted against the shot noise estimate (dotted green line, $R^2 = 0.852$). Solid black lines guide the eye for the measured microbead and QD625 data. Inset (c and d): standard deviations of each barcode σ_{barcode} (black dots) plotted against $\mu_{\text{barcode}}^{1/2}$ with estimates for σ_{particle} (dashed red line) and σ_{shot} (dotted green line). Scatter plots of (e) microbead and (f) QD drop library data scaled by $V^{1/2}$. Clusters identified by DBSCAN are indicated in blue while noise is in black. Missing clusters in (f) are due to two clogged channels in the PIPE chip and are indicated by dotted yellow ovals.

Contributions from spectral crosstalk and sources of noise limit the number of barcodes that can be identified after library reinjection. The narrow emission spectra of QDs leads to less spectral crosstalk between each barcoding color compared to the microbeads. This can be observed in the raw data of the 24 microbead fluorescence intensities (Fig. 4a) compared to the 192 QD fluorescence intensities (Fig. 4b). Due to the wide emission spectra of the microbeads, the emission of the green microbeads overlaps with the red microbeads. This causes barcodes with high green intensity to appear more red, skewing the data to the upper right (Fig. 4a). The effect of spectral crosstalk also skews the QD data (Fig. 4b), but due to the narrow emission spectra of the QDs, the effect is lower in magnitude compared to the microbeads.

We applied a clustering algorithm, Density-Based Spatial Clustering of Applications with Noise (DBSCAN), to identify and separate "clusters" of specific barcoded drops within the libraries.[24] Densely packed data points are assigned to clusters by DBSCAN while outlier data points in low-density regions are marked as noise. When the data are graphed on a linear plot, DBSCAN was able to group 70% of the 1.31×10^4 drops containing microbeads into 24 clusters (Fig. 4a, blue dots) and 30% as noise (Fig. 4a, black dots), with a mean of 399 ± 201 drops per barcode (CV = 50.4%). However, DBSCAN was not able to completely identify clusters in the QD raw data (Fig. 4b, blue dots). Of the clusters identified, DBSCAN grouped 76% of the 1.27×10^5 drops containing QDs with a range of 15 to 6033 drops per barcode (mean of 508 ± 478 drops and CV = 94.1%). A significant number of clusters were mislabeled as noise (Fig. 4b, upper right black dots) due to the large variability in cluster density.

To better understand the variability between barcode clusters, we identify two major sources of variation in our data, both a direct consequence of particle size: Poisson loading for microbeads and shot noise for QDs. The loading of approximately 1 μm diameter fluorescent microbeads into drops is dependent upon Poisson statistics. The fluorescence signal obtained from drops containing microbeads follows a Poisson distribution due to the discrete nature of particle loading in drops.[22] The Poisson distribution is described by the equation:

$$P = \frac{\lambda^k e^{-\lambda}}{k!} \tag{2}$$

where P is the probability distribution of drops that contain k number of particles with a mean number of particles per drop λ. Variability inherent to Poisson loading[22] is represented by the standard deviation of the number of particles in drops $\sigma_{particle} = \lambda^{1/2}$. We plot a representative subset of five red microbead barcodes (Fig. 4c, black dots) corresponding to the clusters in Fig. 4a (dashed red boxes). The subset is compared to estimated Poisson distributions centered around the microbead loading concentrations $\lambda = 33, 83, 149, 232,$ and 333 beads/drop where λ is converted to

voltage using an experimentally verified linear standard curve relating PMT output voltage to microbead concentration (beads/drop, λ) (Fig. S7a†). The probability of microbead distributions (Fig. 4c, dashed red line) closely tracks the PMT voltage measurements of the red microbead data (Fig. 4c, black dots) with $R^2 = 0.931$.

When the particle size is far below the objective resolution, for example in the case of QDs that are approximately 10 nm in diameter, the variability in drop fluorescence is no longer a function of the number of discrete particles in drops, but is instead governed by the shot noise of the PMT. Shot noise is inherent to counting photons with a PMT and contributes to the fluorescence signal in low light environments such as high-speed detection of drop fluorescence.[39,40] We plot the signal distributions of a 12 QD625 barcode subset of the QD barcoded library (Fig. 4d, black dots) corresponding to the clusters outlined in Fig. 4b (dashed green boxes). The Schottky equation approximates shot noise[40,41] in which the standard deviation of the PMT voltage σ_{shot} is proportional to the square root of the mean PMT voltage $\mu_{intensity}$ (see ESI† Schottky equation for details). The subset of QD data is compared to normal distributions defined by $\mu_{intensity}$ and σ_{shot} for each QD barcode. The value of $\mu_{intensity}$ is determined by an experimentally verified linear standard curve relating PMT output voltage to QD concentration (nM) (Fig. S7b, eqn (S1)†). The probability of QD distributions (Fig. 4d, green line) closely tracks the PMT voltage measurements of the QD625 data (Fig. 4d, black dots) with $R^2 = 0.852$.

To demonstrate that the remainder of the experimental microbead and QD barcode data follow either Poisson loading or shot noise, barcode clusters are manually grouped and compared to theoretical estimates of $\sigma_{particle}$ (Fig. 4c and d, inset, dashed red line) and σ_{shot} (Fig. 4c and d, inset, dotted green line, see ESI† Calculation of noise for details). Drop library fluorescence data are manually grouped by drawing lines around each cluster by eye (Fig. S8†) to isolate individual barcode signal populations for each PMT channel. The mean $\mu_{barcode}$ and standard deviation $\sigma_{barcode}$ of the manually-segmented 24 microbead and 192 QD signal distributions are calculated for each PMT channel, yielding 48 and 384 values of $\mu_{barcode}$ and $\sigma_{barcode}$. The $\sigma_{barcode}$ is plotted against $\mu_{barcode}^{1/2}$ for each grouped microbead and QD barcode population (Fig. 4c and d, inset, black dots). The experimental $\sigma_{barcode}$ of the microbeads closely follows the theoretical estimate of particle loading noise $\sigma_{particle}$ (Fig. 4c, inset, dashed red line). The $\sigma_{barcode}$ is approximately an order of magnitude greater than the theoretical estimate of shot noise σ_{shot} (Fig. 4c, inset, dotted green line). Therefore, across all drops, the discrimination of microbead barcode signals is limited by particle loading noise as the dominant source of variation. By contrast, the experimental $\sigma_{barcode}$ of the QDs closely follows the theoretical estimate of shot noise σ_{shot} (Fig. 4d, inset, dotted green line) and is approximately an order of magnitude greater than the estimate of particle loading

noise $\sigma_{particle}$ (Fig. 4d, inset, dashed red line), indicating the data is shot noise-limited. The narrow emission spectrum of the QDs results in a 1–2 log decrease of σ_{shot} compared to $\sigma_{particle}$. This enables an 8× increase in unique barcode concentrations obtained with QDs compared to microbeads (192 versus 24).

As signal variation depends upon Poisson loading for microbeads ($\sigma_{particle} \propto \lambda^{1/2}$) and shot noise for QDs ($\sigma_{shot} \propto \mu^{1/2}$), scaling the intensity data for both barcode libraries by a square root function linearizes the noise. This scaling spaces each barcode grouping as shown in Fig. 4e and f (Fig. S5 and S6†). When DBSCAN is applied to the scaled data, the increased spacing allows for improved clustering of each barcode compared to the unscaled raw data (Fig. 4a and b). Of the 1.31×10^4 microbead barcoded drops detected, DBSCAN was able to group 74.8% of the data into 24 clusters (Fig. 4e, blue dots) and identify 25.2% as noise (Fig. 4e, black dots) with a mean of 408 ± 62 drops per barcode (CV = 15.2%). The CV of clustered square root scaled data is greatly reduced from 50.4% with the linearly scaled data (Fig. 4a) to 15.2% with the square root scaled data (Fig. 4e). Additionally, a square root scaling of the QD data allows DBSCAN to correctly identify 188 out of the 192 of barcoded drop populations where the missing four populations are due to two clogged drop makers on the PIPE chip and are indicated by the yellow ovals (Fig. 4f). Of the 1.27×10^5 QD barcoded drops detected, DBSCAN was able to group 85.4% of data into 188 clusters (Fig. 4f, blue dots) and

identify 14.6% as noise (Fig. 4f, black dots) with a mean barcode cluster size of 576 ± 88 drops (CV = 15.3%). Once again, the CV is greatly reduced from 94.1% with the linearly-scaled quantum dot data to 15.5% with the square root-scaled data.

Previous examples of drop libraries using one or two fluorescence dye colors have realized up to eight[10] or sixteen[11] unique labels. Using the PIPE chip, we achieved a total of 188 discrete barcodes with two-color combinations of QDs. To our knowledge, this is the largest two-color fluorescent barcode combination in drops to date. Additionally, the effect of particle size on signal noise can be described empirically and used for future experiments to inform the selection of barcode concentrations.

Sample isolation using fluorescence-activated drop sorting

To demonstrate the utility of the PIPE chip, fluorescence-activated drop sorting[21,22] was performed to isolate drops of a single barcode population within a drop library of 24 green and red microbead combinations spiked with four concentrations of blue microbeads. We verify that the desired green and red barcode combination was isolated by detecting a single concentration of the blue microbeads. A barcode from the drop library was chosen by designating a box with upper and lower fluorescence intensity bounds in the green and red fluorescence channels (Fig. 5a, red box). Recovery of
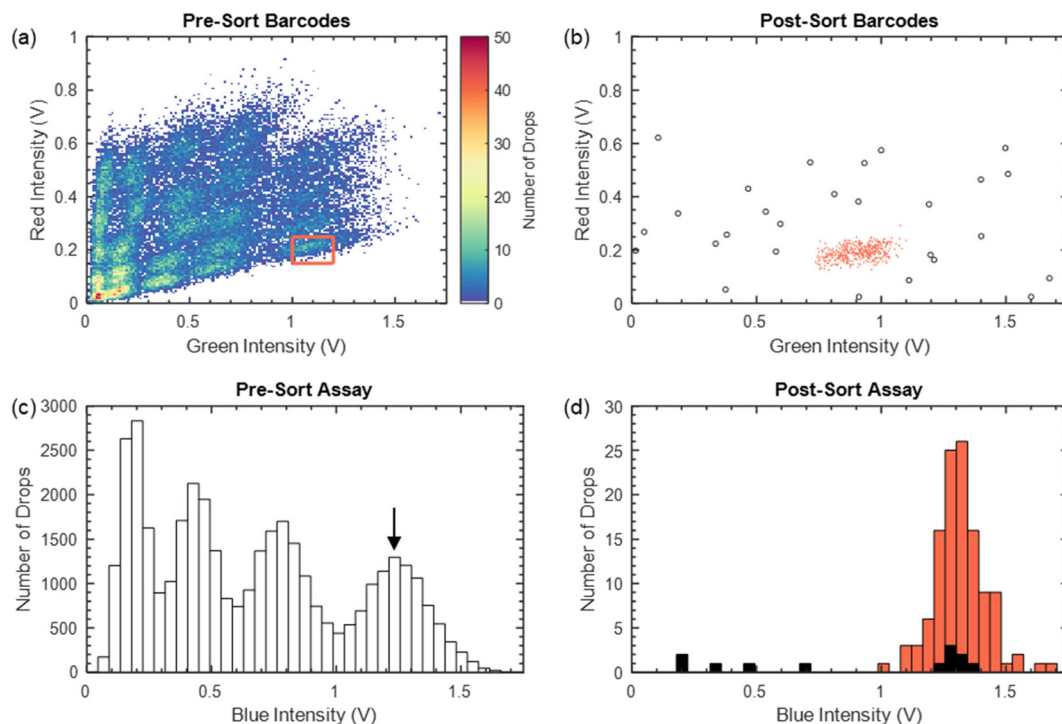

Fig. 5 Fluorescence-activated drop sorting of a microbead-barcoded drop library. (a) Fluorescence intensity of barcoded drops before sorting. The sorted region is indicated by the red box. (b) Fluorescence intensity of barcoded drops after sorting. DBSCAN is used to separate the outlier data points (open black circles) from the target barcode population (red dots). (c) Distribution of four concentrations of blue microbead drops within the drop library. (d) Distribution of blue microbeads in the sorted barcoded drop population shows a single peak corresponding to the largest concentration of blue microbeads. DBSCAN is used to separate the outliers (black bars) from the target sorted population (red bars).

the desired barcode population is confirmed by performing flow-based fluorescence detection on the sorted drops, yielding an isolated barcode cluster with intensity bounds close to those originally chosen in the green and red channels (Fig. 5b). However, there is an observed shift in fluorescence signal distribution from pre- to post-sort (Fig. 5a and b) where the post-sort data has shifted by ≈0.2 V along the *x*-axis. This shift is likely caused by run-to-run variation arising from the positioning of the laser in the device channel. Post-processing of the sorted drop data using DBSCAN provides a clear distinction between the target barcode population (Fig. 5b, red dots) and the outlier data points (Fig. 5b, open black circles). The outlier points comprise 7.5% of the drop data.

The four populations of blue microbead-barcoded drops were detected in the pre-sort drop library (Fig. 5c). Fluorescence detection of the sorted drops yielded a single blue microbead population with few outliers (Fig. 5d), matching the highest blue microbead concentration (Fig. 5c, arrow). DBSCAN clustering of corresponding green and red fluorescence identifies these outliers (Fig. 5d, black bars) and the target sorted population (Fig. 5d, red bars). The outliers comprise 5.9% of the sorted population, in close agreement with the data corresponding to the green and red barcoded drops (Fig. 5b). These results demonstrate the ability to isolate a single barcoded population from a drop library created using the PIPE chip, critical for performing downstream assays.

Conclusions

Here we have demonstrated tunable parallel production of 50 to 90 μm diameter drops containing upwards of 96 different loading conditions from a microtiter plate, improving upon the previously published limit of 24.[20] By scaling the signal noise with the square root of the intensity, barcoded drop libraries comprised of 24 microbead barcodes or 192 QD barcodes are distinguishable using DBSCAN.[24] Barcode number is ultimately limited by microbead or QD signal resolution. As a function of size, signal resolution between larger microbeads was limited by Poisson loading noise while the signals from the smaller QD barcodes were limited by shot noise. This empirical relationship found between signal noise and barcode concentration can be used to quickly prototype barcode label concentrations for future experiments. Utilizing two-color combinations of QDs, we achieved a total of 188 discrete barcodes, the largest two-color fluorescence barcode combination in drops published to date. The addition of a third QD color, offering up to 16 unique concentrations, would enable QDs to easily index multiple 384-well microtiter plates using as many as 3072 unique barcodes (12 × 16 × 16), far surpassing what has been achieved with four color combinations (1050 labels).[4] Furthermore, we have shown that barcoded populations can be selectively sorted with minimal error (5.9–7.5%), demonstrating that downstream analysis of a specific sample population is possible. By reducing sample encapsulation time and enabling rapid, parallel generation of a barcoded library directly from a microtiter plate, we envision that the PIPE chip will further advance multiplexed assaying in applications including combinatorial drug screening,[3,10] DNA microarray analysis,[11] or enzyme activity screening.[12]

Author contributions

Conflicts of interest

There are no conflicts to declare.

Acknowledgements

References

1 J. J. Agresti, E. Antipov, A. R. Abate, K. Ahn, A. C. Rowat, J.-C. Baret, M. Marquez, A. M. Klibanov, A. D. Griffiths and D. A. Weitz, *Proc. Natl. Acad. Sci. U. S. A.*, 2010, **107**, 4004–4009.

2 M. T. Guo, A. Rotem, J. A. Heyman and D. A. Weitz, *Lab Chip*, 2012, **12**, 2146–2155.

3 A. Kulesa, J. Kehe, J. E. Hurtado, P. Tawde and P. C. Blainey, *Proc. Natl. Acad. Sci. U. S. A.*, 2018, **115**, 6685–6690.

4 C. M. Ackerman, C. Myhrvold, S. G. Thakku, C. A. Freije, H. C. Metsky, D. K. Yang, H. Y. Simon, C. K. Boehm, T.-S. F. Kosoko-Thoroddsen and J. J. N. Kehe, *Nature*, 2020, 1–6.

5 O. Scheler, K. Makuch, P. R. Debski, M. Horka, A. Ruszczak, N. Pacocha, K. Sozański, O.-P. Smolander, W. Postek and P. J. S. R. Garstecki, *Sci. Rep.*, 2020, **10**, 1–8.

6 A. M. Klein, L. Mazutis, I. Akartuna, N. Tallapragada, A. Veres, V. Li, L. Peshkin, D. A. Weitz and M. W. J. C. Kirschner, *Cell*, 2015, **161**, 1187–1201.

7 A. Rotem, O. Ram, N. Shoresh, R. A. Sperling, A. Goren, D. A. Weitz and B. E. Bernstein, *Nat. Biotechnol.*, 2015, **33**, 1165–1172.

8 A. Rotem, O. Ram, N. Shoresh, R. A. Sperling, M. Schnall-Levin, H. Zhang, A. Basu, B. E. Bernstein and D. A. Weitz, *PLoS One*, 2015, **10**, e0116328.

9 E. Z. Macosko, A. Basu, R. Satija, J. Nemesh, K. Shekhar, M. Goldman, I. Tirosh, A. R. Bialas, N. Kamitaki and E. M. Martersteck, *Cell*, 2015, **161**, 1202–1214.

10 E. Brouzes, M. Medkova, N. Savenelli, D. Marran, M. Twardowski, J. B. Hutchison, J. M. Rothberg, D. R. Link, N. Perrimon and M. L. Samuels, *Proc. Natl. Acad. Sci. U. S. A.*, 2009, **106**, 14195–14200.

11 A. R. Abate, T. Hung, R. A. Sperling, P. Mary, A. Rotem, J. J. Agresti, M. A. Weiner and D. A. Weitz, *Lab Chip*, 2013, **13**, 4864–4869.

12 C. H. Chen, M. A. Miller, A. Sarkar, M. T. Beste, K. B. Isaacson, D. A. Lauffenburger, L. G. Griffith and J. Han, *J. Am. Chem. Soc.*, 2013, **135**, 1645–1648.

13 J. Kehe, A. Kulesa, A. Ortiz, C. M. Ackerman, S. G. Thakku, D. Sellers, S. Kuehn, J. Gore, J. Friedman and P. C. Blainey, *Proc. Natl. Acad. Sci. U. S. A.*, 2019, **116**, 12804–12809.

14 O. J. Miller, A. El Harrak, T. Mangeat, J. C. Baret, L. Frenz, B. El Debs, E. Mayot, M. L. Samuels, E. K. Rooney, P. Dieu, M. Galvan, D. R. Link and A. D. Griffiths, *Proc. Natl. Acad. Sci. U. S. A.*, 2012, **109**, 378–383.

15 T. S. Kaminski, S. Jakiela, M. A. Czekalska, W. Postek and P. Garstecki, *Lab Chip*, 2012, **12**, 3995–4002.

16 T. D. Rane, H. C. Zec and T.-H. Wang, *J. Lab. Autom.*, 2012, **17**, 370–377.

17 J. Clausell-Tormos, A. D. Griffiths and C. A. Merten, *Lab Chip*, 2010, **10**, 1302–1307.

18 M.-P. N. Bui, C. A. Li, K. N. Han, J. Choo, E. K. Lee and G. H. Seong, *Anal. Chem.*, 2011, **83**, 1603–1608.

19 J. Lim, O. Caen, J. Vrignon, M. Konrad, V. Taly and J.-C. Baret, *Biomicrofluidics*, 2015, **9**, 034101.

20 L. A. Bawazer, C. S. McNally, C. J. Empson, W. J. Marchant, T. P. Comyn, X. Niu, S. Cho, M. J. McPherson, B. P. Binks, A. deMello and F. C. Meldrum, *Sci. Adv.*, 2016, **2**, e1600567.

21 J. C. Baret, O. J. Miller, V. Taly, M. Ryckelynck, A. El-Harrak, L. Frenz, C. Rick, M. L. Samuels, J. B. Hutchison, J. J. Agresti, D. R. Link, D. A. Weitz and A. D. Griffiths, *Lab Chip*, 2009, **9**, 1850–1858.

22 L. Mazutis, J. Gilbert, W. L. Ung, D. A. Weitz, A. D. Griffiths and J. A. Heyman, *Nat. Protoc.*, 2013, **8**, 870–891.

23 P. Gruner, B. Riechers, B. Semin, J. Lim, A. Johnston, K. Short and J.-C. Baret, *Nat. Commun.*, 2016, **7**, 1–9.

24 M. Ester, H.-P. Kriegel, J. Sander and X. Xu, *A density-based algorithm for discovering clusters in large spatial databases with noise*, Portland, OR, 1996.

25 S. W. Lim, T. M. Tran and A. R. Abate, *PLoS One*, 2015, **10**, e0113549.

26 H. Zhang, S. K. Cockrell, A. O. Kolawole, A. Rotem, A. W. Serohijos, C. B. Chang, Y. Tao, T. S. Mehoke, Y. Han and J. S. Lin, *J. Virol.*, 2015, **89**, 7722–7734.

27 Y. Tao, A. Rotem, H. Zhang, S. K. Cockrell, S. A. Koehler, C. B. Chang, L. W. Ung, P. G. Cantalupo, Y. Ren and J. S. J. C. Lin, *ChemBioChem*, 2015, **16**, 2167–2171.

28 C. Holtze, A. C. Rowat, J. J. Agresti, J. B. Hutchison, F. E. Angile, C. H. Schmitz, S. Koster, H. Duan, K. J. Humphry, R. A. Scanga, J. S. Johnson, D. Pisignano and D. A. Weitz, *Lab Chip*, 2008, **8**, 1632–1639.

29 C. H. Schmitz, A. C. Rowat, S. Köster and D. A. Weitz, *Lab Chip*, 2009, **9**, 44–49.

30 T. Cubaud and T. G. Mason, *Phys. Fluids*, 2008, **20**, 053302.

31 J. D. Tice, A. D. Lyon and R. F. Ismagilov, *Anal. Chim. Acta*, 2004, **507**, 73–77.

32 D. Funfschilling, H. Debas, H.-Z. Li and T. Mason, *Phys. Rev. E: Stat., Nonlinear, Soft Matter Phys.*, 2009, **80**, 015301.

33 P. Garstecki, H. A. Stone and G. M. Whitesides, *Phys. Rev. Lett.*, 2005, **94**, 164501.

34 P. Garstecki, M. J. Fuerstman, H. A. Stone and G. M. Whitesides, *Lab Chip*, 2006, **6**, 437–446.

35 A. Abate, A. Poitzsch, Y. Hwang, J. Lee, J. Czerwinska and D. Weitz, *Phys. Rev. E: Stat., Nonlinear, Soft Matter Phys.*, 2009, **80**, 026310.

36 H. Q. Nguyen, B. C. Baxter, K. Brower, C. A. Diaz-Botia, J. L. DeRisi, P. M. Fordyce and K. S. Thorn, *Adv. Opt. Mater.*, 2017, **5**, 1600548.

37 M. Han, X. Gao, J. Z. Su and S. Nie, *Nat. Biotechnol.*, 2001, **19**, 631.

38 H. Lee, J. Kim, H. Kim, J. Kim and S. Kwon, *Nat. Mater.*, 2010, **9**, 745–749.

39 A. Huebner, M. Srisa-Art, D. Holt, C. Abell, F. Hollfelder, A. Demello and J. J. C. C. Edel, *Chem. Commun.*, 2007, 1218–1220.

40 R. L. McClain and J. C. Wright, *J. Chem. Educ.*, 2014, **91**, 1455–1457.

41 W. Schottky, *Ann. Phys.*, 1918, **362**, 541–567.